Supplementary material

Impacts of subgrid elevation bands on hydrological portrayals: insights from a suite of hydroclimatically diverse mountainous catchments

Octavio Murillo[1], Pablo A. Mendoza[1,2], Nicolás Vásquez[1], Naoki Mizukami[3] and Álvaro Ayala[4]

[1]Department of Civil Engineering, Universidad de Chile, Santiago, Chile.

[2]Advanced Mining Technology Center (AMTC), Universidad de Chile, Santiago, Chile.

[3]National Center for Atmospheric Research (NCAR), Boulder, Colorado, USA.

[4]Centro de Estudios Avanzados en Zonas Áridas (CEAZA), La Serena, Chile.

Corresponding author: Pablo Mendoza (pamendoz@uchile.cl)

Keywords: Elevation bands, vertical discretization, VIC, spatial heterogeneity, snow water equivalent

1. Content

This supplementary material file contains additional figures and tables to support the analysis of the results presented in the main manuscript. The methodology used to obtain these results is explained in the main manuscript.

The following sections are presented:

2. Attributes for catchment selection

Table S1 shows the attributes used in this study for basin selection, including the glacier area, the intervention degree (relationship between annual volume of water assigned as permanent consumptive rights and the mean annual flow) and the presence of big dams.

Table S1: Attributes for the case study basins included here, and used for the catchment selection process (Alvarez-Garreton et al., 2018).

Catchment	Glacier area (%)	Intervention degree (%)	Big dams
Estero Pocuro en el Sifón	0	0	No
Estero Arrayán en la Montosa	0	5.78	No
Río Mapocho en Los Almendros	0.73	0.27	No
Río Las Leñas antes junta Río Cachapoal	0.45	0	No
Río Claro en El Valle	0	0.05	No
Río Colorado en junta con Palos	0.72	0	No
Río Palos en junta con Colorado	0.02	< 0.01	No
Río Melado en el Salto	0.97	< 0.01	No
Río Ñuble en La Punilla	1.09	0.26	No

3. Observed time series for selected catchments

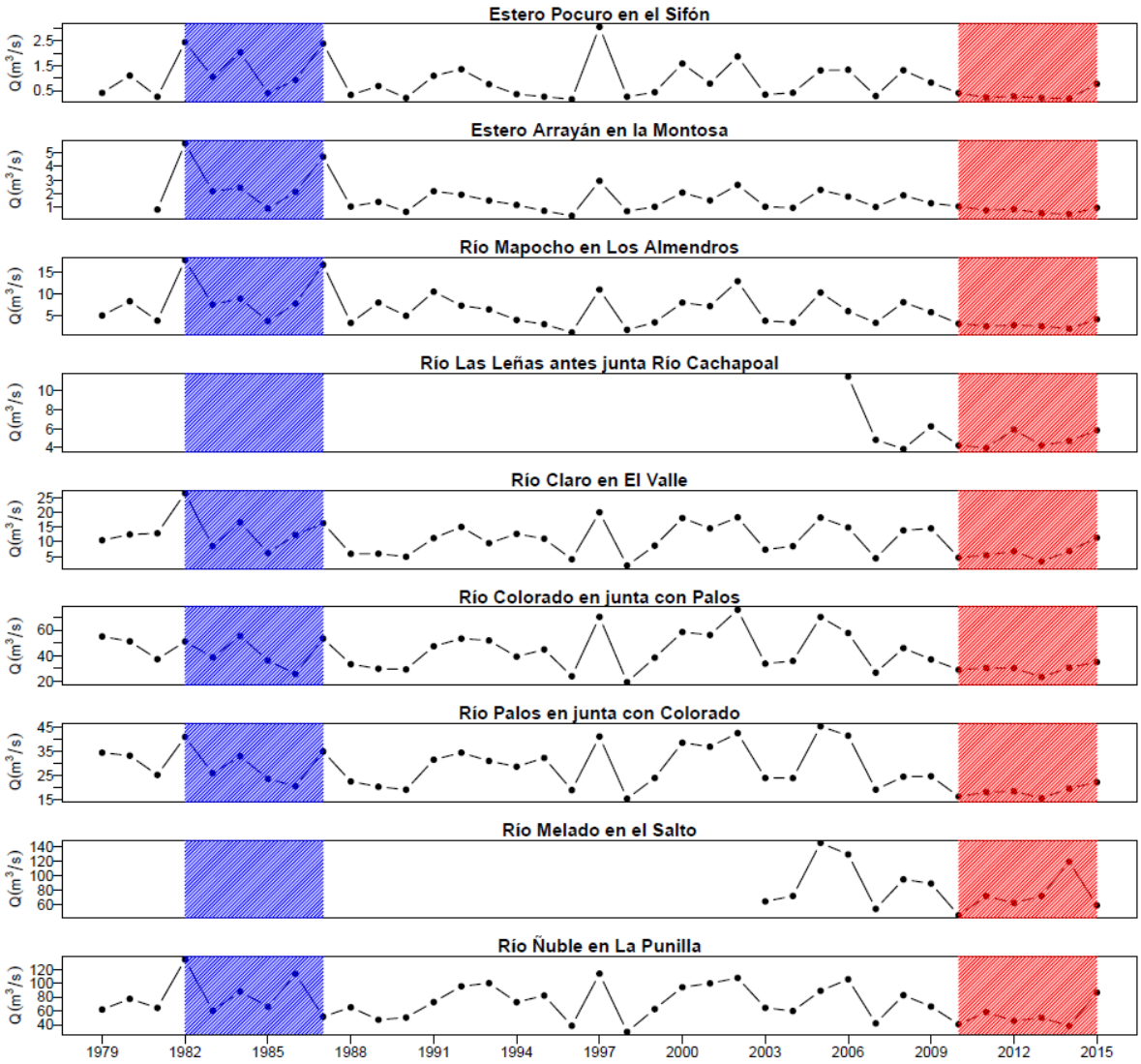

Figure S1: Time series of mean annual streamflow for the climatological period. The blue shaded region represents the wet period (April/1982 – March/1986). Red shaded subperiod represents the dry period (April/2010 – March/2014).

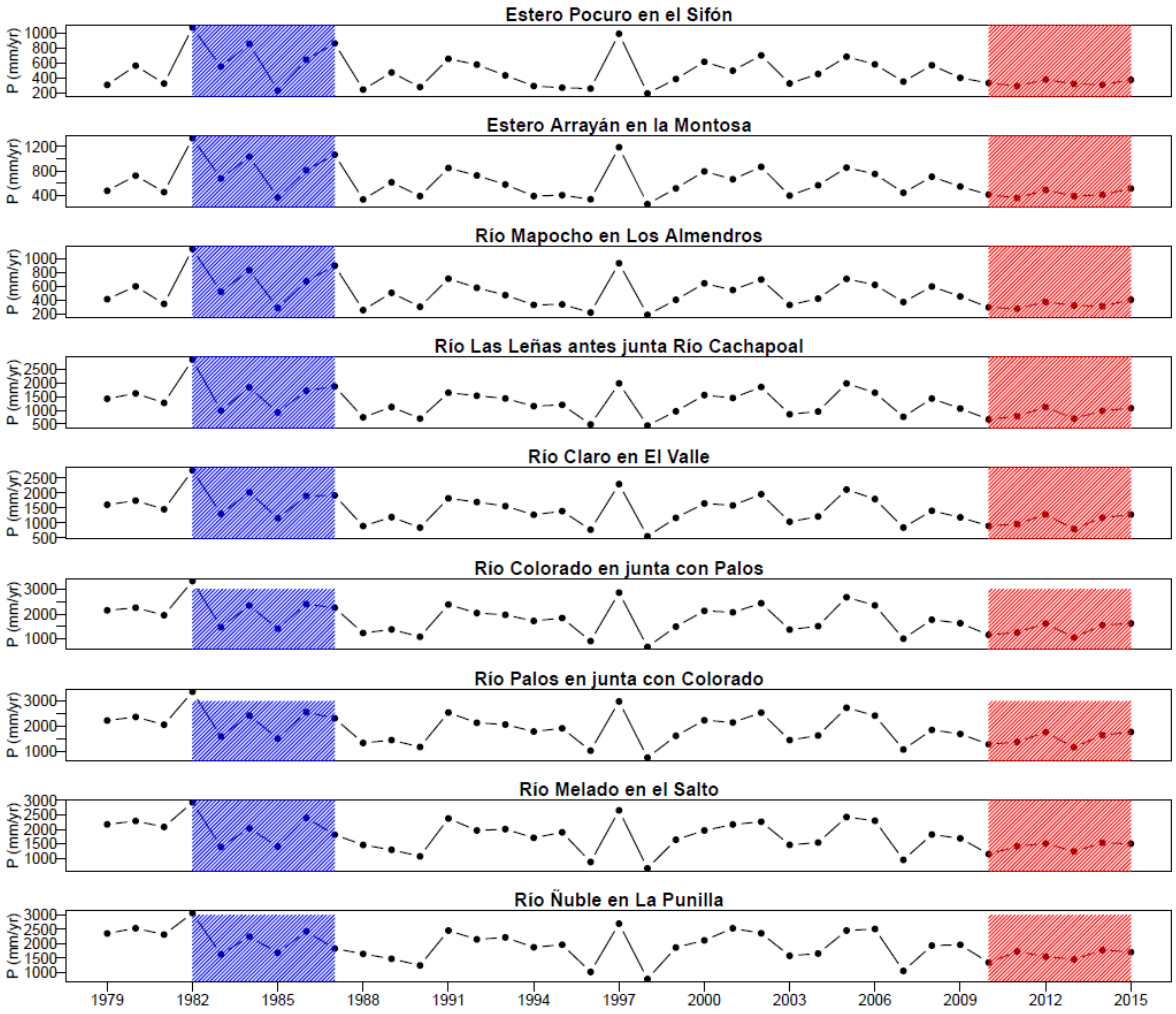

Figure S2: Time series of annual precipitation for the climatological period. The blue shaded region represents the wet period (April/1982 – March/1986). Red shaded subperiod represents the dry period (April/2010 – March/2014).

4. NSE and KGE components

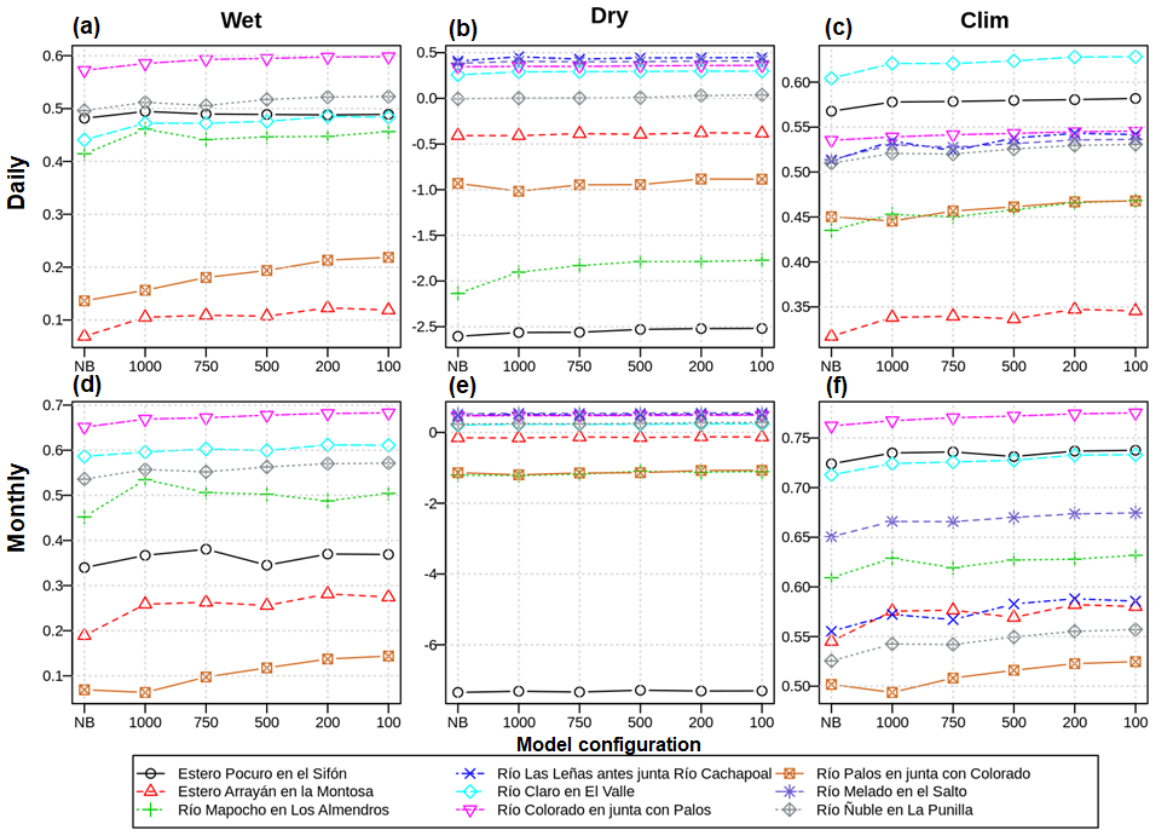

Figure S3: NSE results computed with daily (top) and monthly (bottom) runoff, obtained from the benchmark (NB: No Bands) and the five alternative model configurations (i.e., using 1000-m, 750-m, 500-m, 200-m, and 100-m elevation bands). Each curve displays individual basin results, and missing basins in some panels indicate the absence of verification (i.e., observed) data for that period.

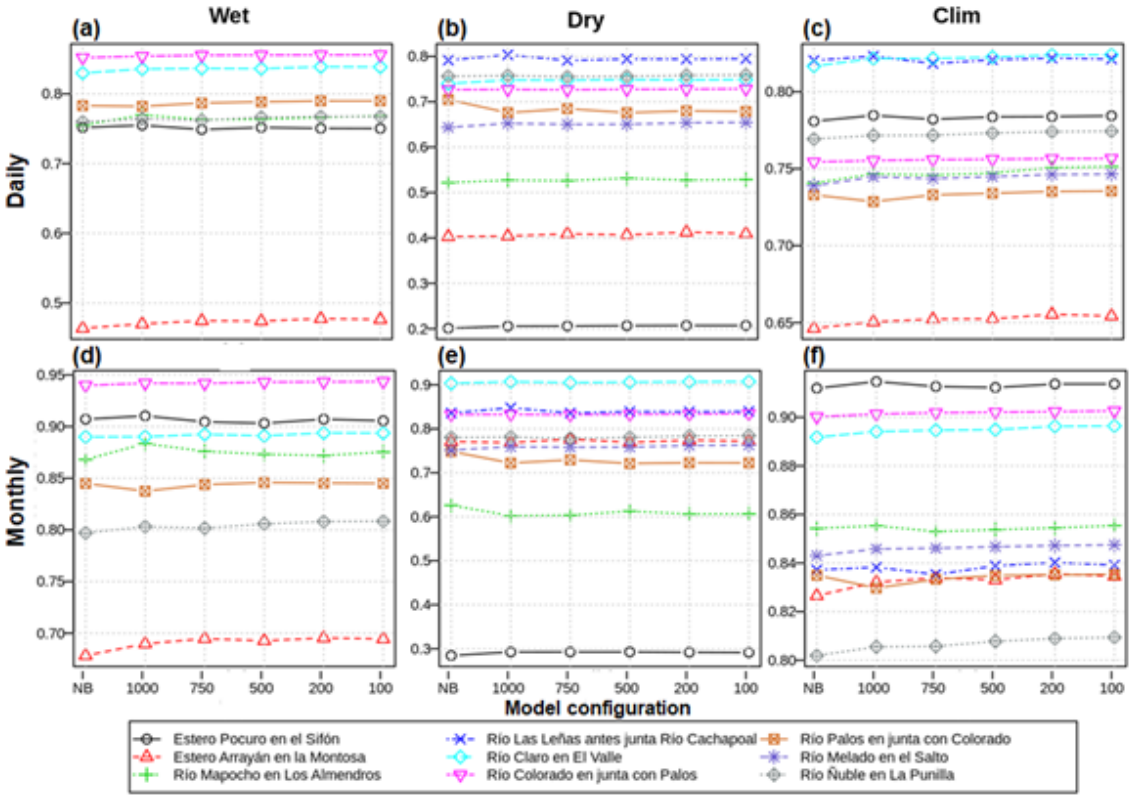

Figure S4: Pearson product-moment correlation coefficient between simulated and observed runoff. The results are displayed for daily (top) and monthly (bottom) runoff, obtained from the benchmark (NB: No Bands) and the five alternative model configurations (i.e., using 1000-m, 750-m, 500-m, 200-m, and 100-m elevation bands). Each curve displays individual basin results, and missing basins in some panels indicate the absence of verification (i.e., observed) data for that period.

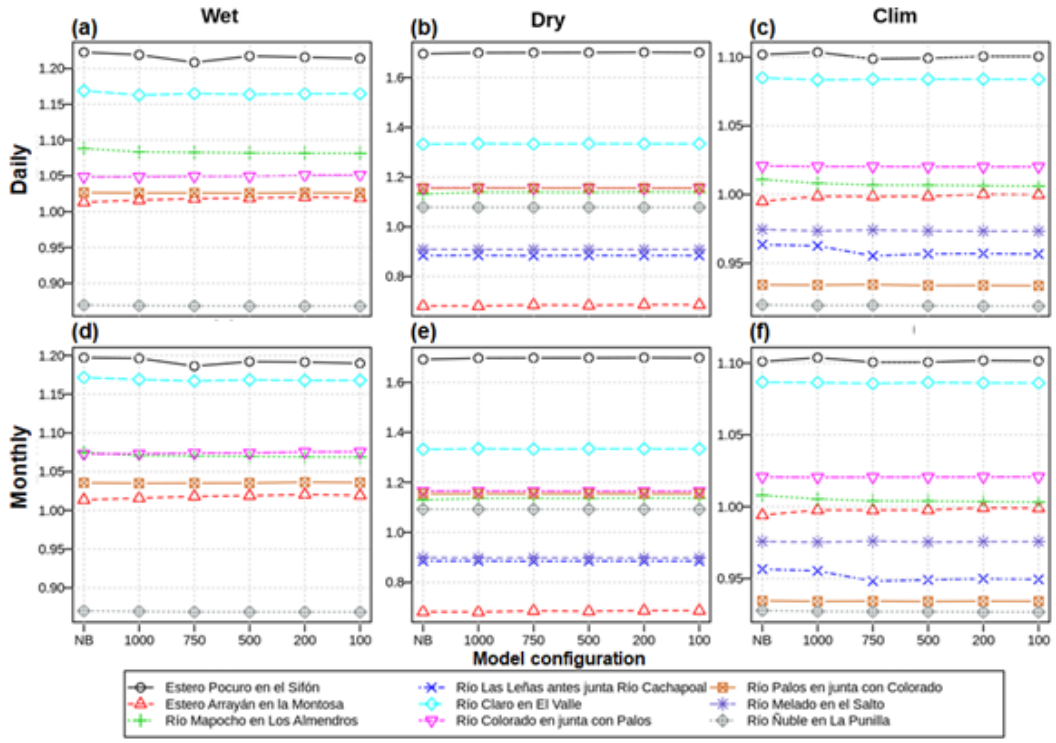

Figure S5: Same as in S12, but for the ratio β between the mean of the simulated values to the mean of observations.

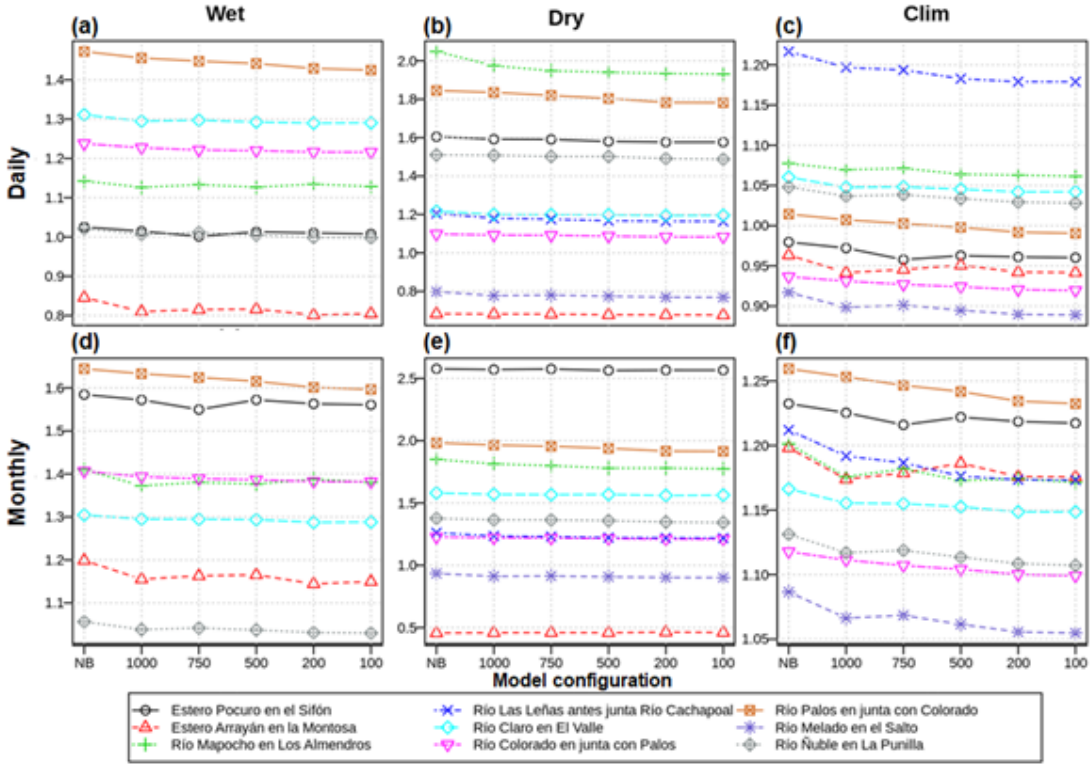

Figure S6: Same as in S12, but for the ratio α of the standard deviation of simulated values to the standard deviation of observed values.

5. Spatial heterogeneity of water balance variables

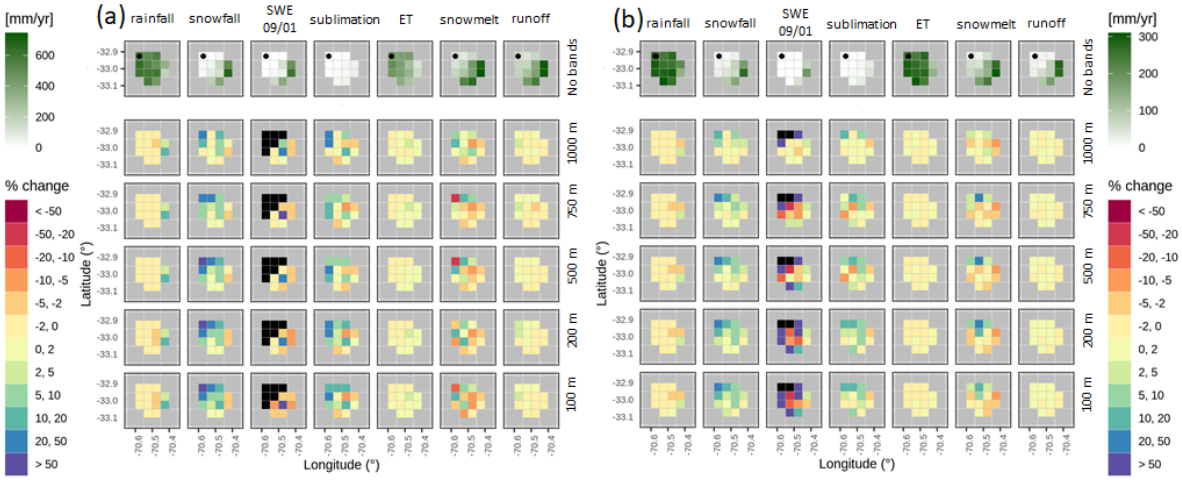

Figure S7: Spatial variability of percent changes [100*(alternative – benchmark)/benchmark] in grid cell-scale simulated mean annual fluxes and SWE 09/01 at the Pocuro River basin. Results are presented for (a) wet and (b) dry analysis periods. The various columns display, from left to right, results for mean annual rainfall, mean annual snowfall, mean SWE 09/01, mean annual sublimation, mean annual ET, mean annual snowmelt and mean annual runoff. The top row displays results for the benchmark model in mm/yr (excepting SWE 09/01, presented in mm), while the remaining rows show results for alternative model configurations (i.e., 1000, 750, 500, 200 and 100 m elevation bands, from top to bottom). Black tiles indicate no data, associated with benchmark model results equal to zero (or unbounded result). The black dot in the top row represents the catchment outlet.

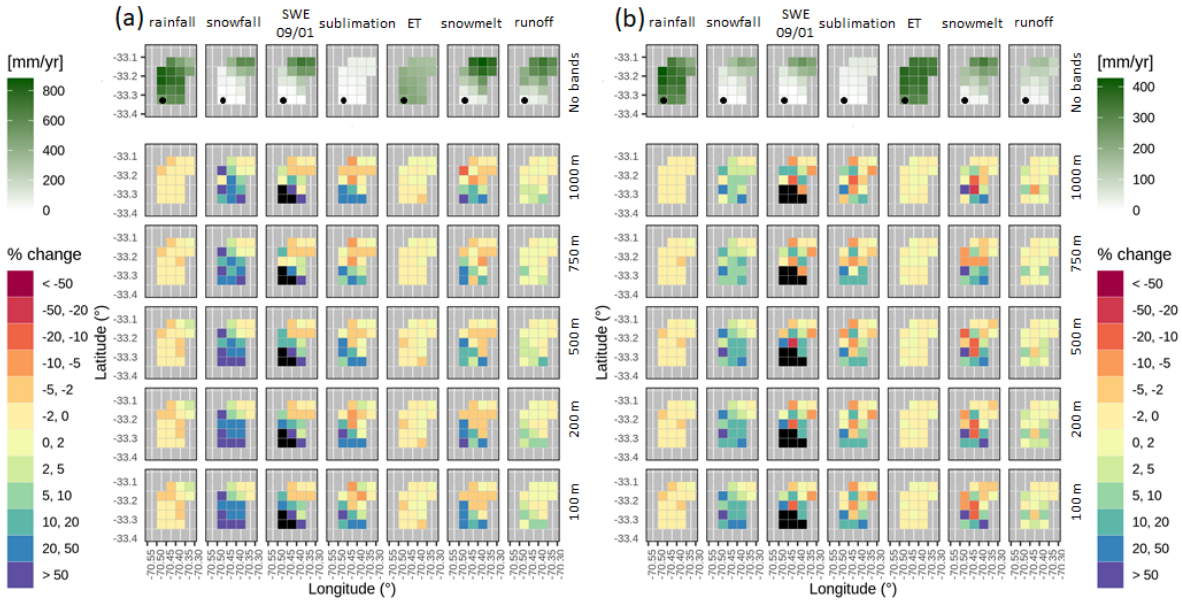

Figure S8: Same as in Figure S7, but for Estero Arrayán en la Montosa

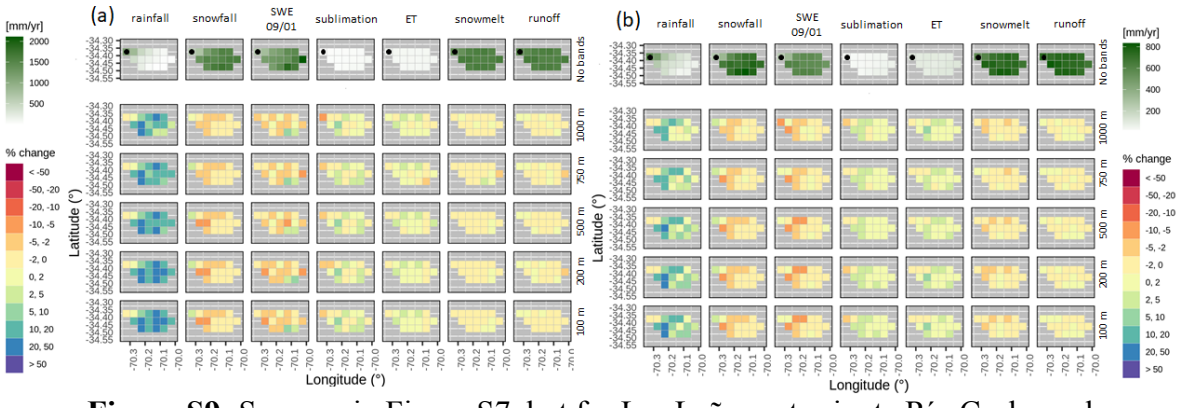

Figure S9: Same as in Figure S7, but for Las Leñas antes junta Río Cachapoal

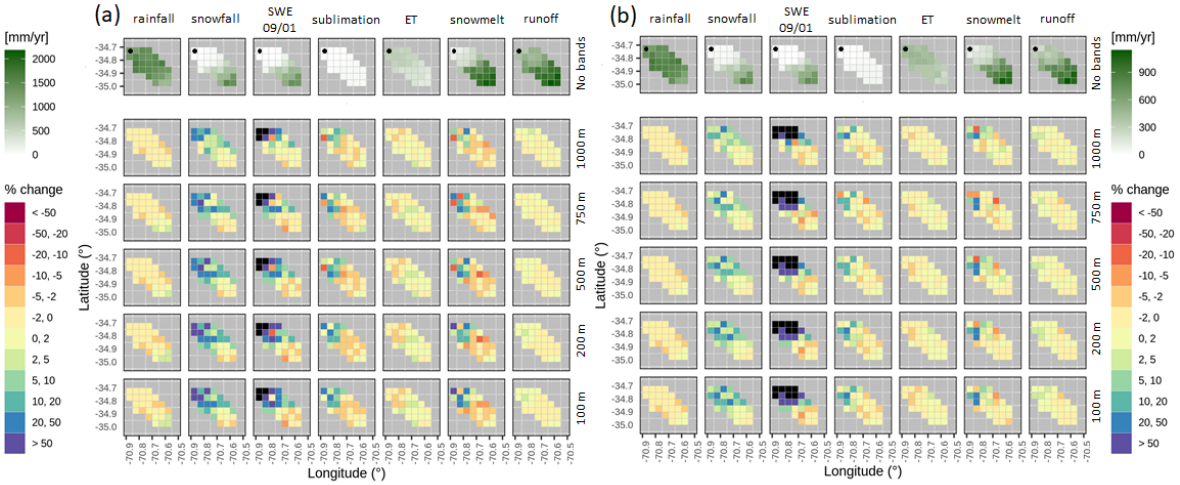

Figure S10: Same as in Figure S7, but for Río Claro en El Valle.

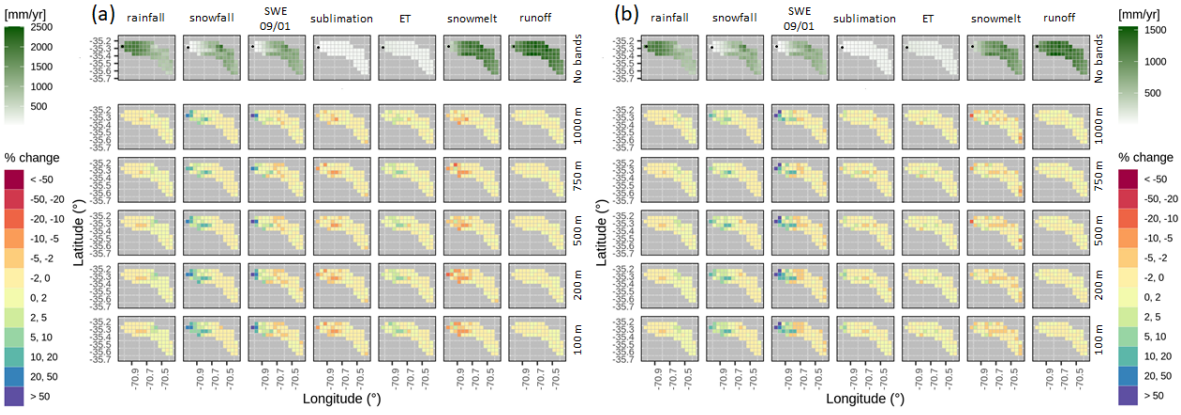

Figure S11: Same as in Figure S7, but for Río Colorado en junta con Palos.

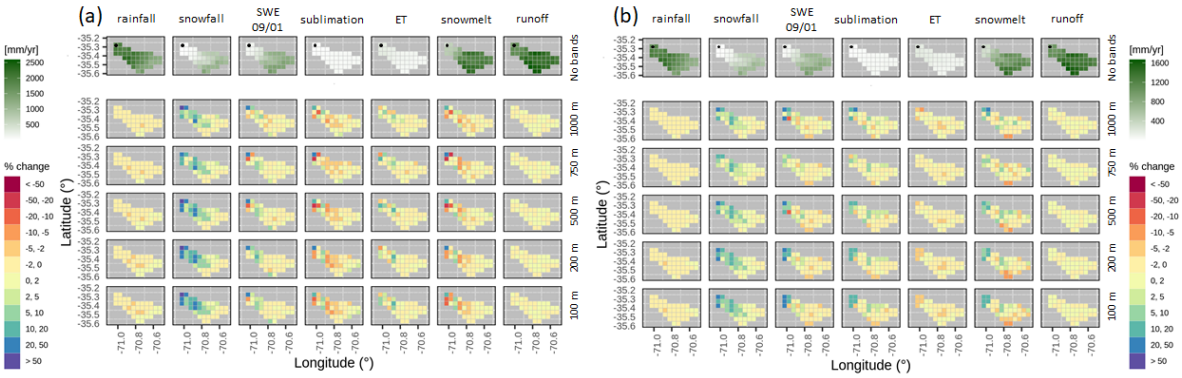

Figure S12: Same as in Figure S7, but for Río Palos en junta con Colorado.

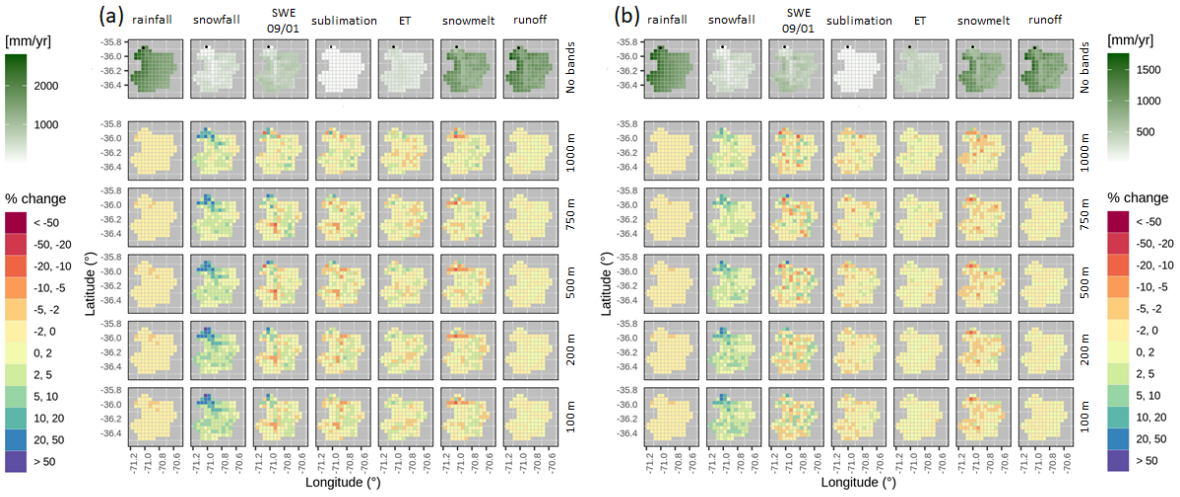

Figure S13: Same as in Figure S7, but for Río Melado en El Salto.

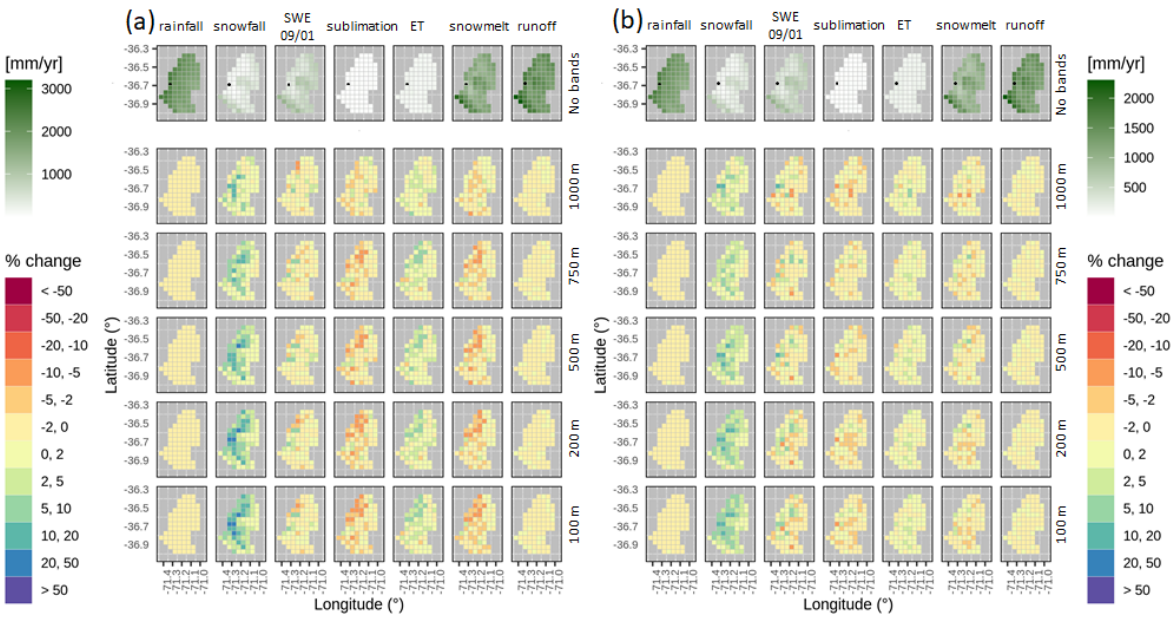

Figure S14: Same as in Figure S4, but for Río Ñuble en La Punilla.

6. Energy Balance

In this section, we provide details on the energy balance approach implemented in VIC, and the results obtained for the basins of interest.

VIC computes the albedo using the United States Army Corps of Engineers method (USACE, 1956), which is an empirical equation for albedo decay, where this variable depends on the age of snow surface. Therefore, snow albedo is not directly affected by air temperature.

In VIC, the cloudiness and its effect on radiation is calculated using equations 2.29 from Bras (1990) and the method of Deardorff (1978). Part of the code used by VIC for processing atmospheric data comes from MT-CLIM, which is a weather preprocessor developed by the NTSG group in the School of Forestry at the University of Montana.

The longwave radiation, which can be succinctly described in terms of an emissivity, was calculated using the Prata parametrization (1996):

$$\varepsilon = 1 - (1 + \xi) exp\ (-\sqrt{1.2 + 3.0\xi}) \quad (1)$$

$$\xi = \left(\frac{e_0}{T_0}\right)\left(\frac{M_w}{R^* k \psi}\right) \quad (2)$$

$$\psi = 1 + \left(\frac{e}{p}\right)\frac{M_w}{M_a} \quad (3)$$

$$k = k_w + \frac{\gamma}{\overline{T_0}} \quad (4)$$

where:
ε: clear-sky emissivity
e_0: screen-level value of the vapor pressure.
e: partial pressure of water vapor.
T_0: measured temperature.
γ: temperature lapse rate.
M_w and M_a are the molecular weight of water vapor and dry air, respectively.
R^*: universal gas constant ($R^* = 8.314 \cdot 10^3 Jkg^{-1}kmol^{-1}$)

In equation (1), the overbar represents the mean value.

The incident solar radiation is obtained iteratively, using the equations by Thornton & Running (1999).

Canopy temperature is obtained by iteratively solving the canopy-atmosphere and canopy-ground exchange fluxes (e.g., turbulent fluxes).

Figures S15-S23 show the spatial heterogeneity obtained with the benchmark model for the net radiation at the surface (including longwave and shortwave radiation), latent and sensible heat fluxes from the surface and the ground heat flux plus heat storage in the top soil layer. Additionally, the intra-catchment variability

of changes induced by different subgrid discretizations is also illustrated. The key findings of these figures are as follows:

- In general, the results show that incorporating elevation bands does not yield variations of net radiation larger than 10% in any basin, during both analysis periods (except in Figure S15, for an only grid cell). Further, the effects of increasing the number of elevation bands in all basins seem to be moderate.

- In some basins, the latent heat flux gets reduced near the catchment outlets (e.g. Figure S15a, Figure S17a, Figure S19a, Figure S21b), while in others larger reductions are obtained at high elevations (e.g. Figure S20a, Figure S21a, Figure S23a). In general, elevation bands provide the largest variations for this variable during the wet period.

- The results show that elevation bands yield reductions in sensible heat flux at the highest altitude grid cells (e.g. Figure S15, Figure S18). Again, the largest variations occur during the wet period (specially in Las Leñas basin, Figure S18a).

- Finally, elevation bands yield increased ground heat flux near the catchment outlets, and also reductions that mostly occur in high elevation grid cells (e.g., Figure S15, Figure S17b, Figure S19, Figure S21b). For some basins and configurations, the largest decrease in ground heat flux is obtained at the lowest altitude grid cell (e.g., Figure S16a, Figure S17a, Figure S18, Figure S19a, Figure S21a).

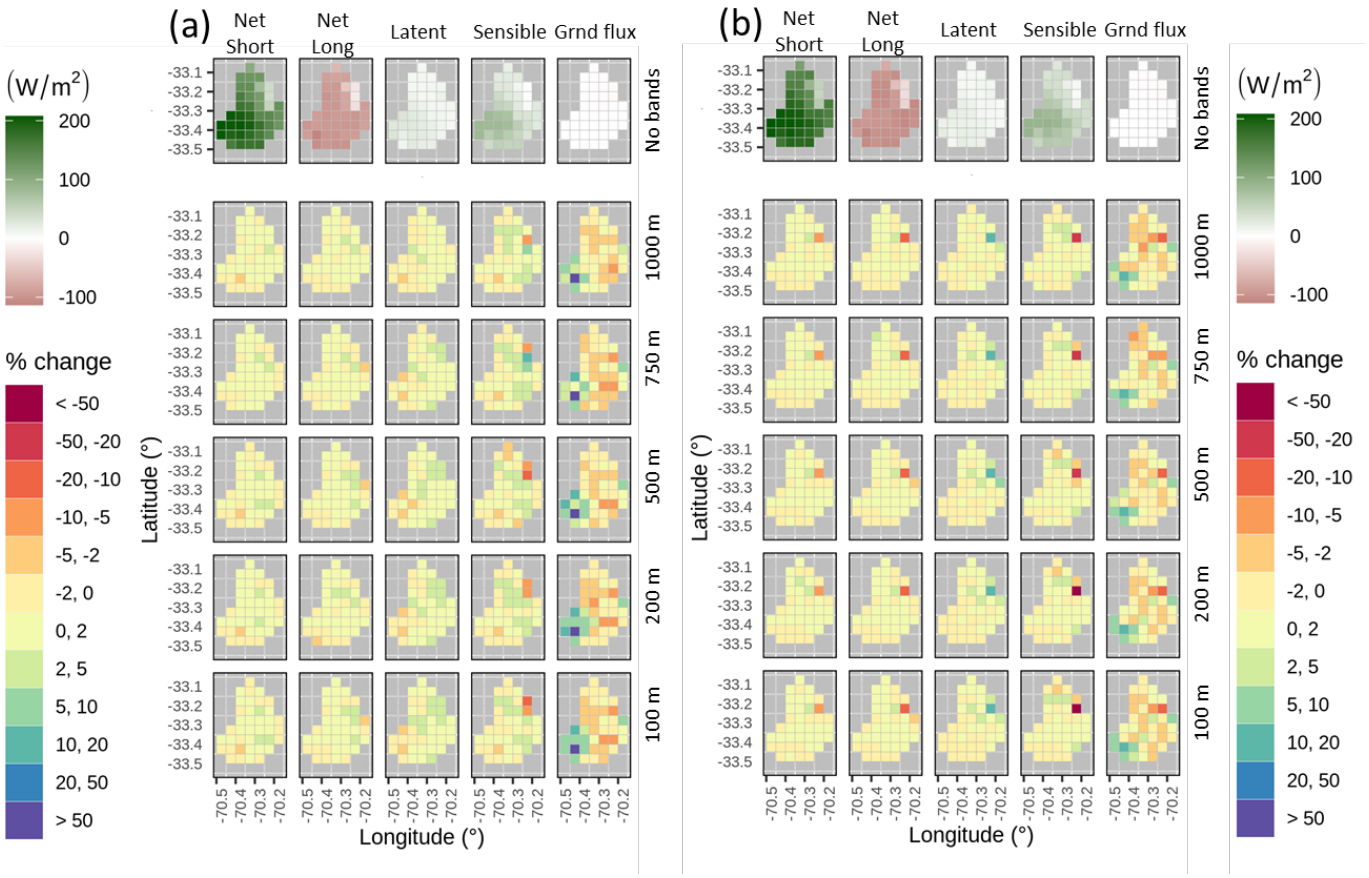

Figure S15: Spatial variability of percent changes [100·(alternative – benchmark)/benchmark] in grid cell-scale simulated mean annual energy fluxes at the Mapocho en Los Almendros basin. Results are presented for (a) wet and (b) dry analysis periods. The various columns display, from left to right, net shortwave, net longwave, latent and sensible heat fluxes from the surface and ground heat flux plus heat storage in the top soil layer. The top row displays results for the benchmark model in W/m^2, while the remaining rows show results for alternative model configurations (i.e., 1000, 750, 500, 200 and 100 m elevation bands, from top to bottom). Black tiles indicate no data, associated to benchmark model results equal to zero (or unbounded result).

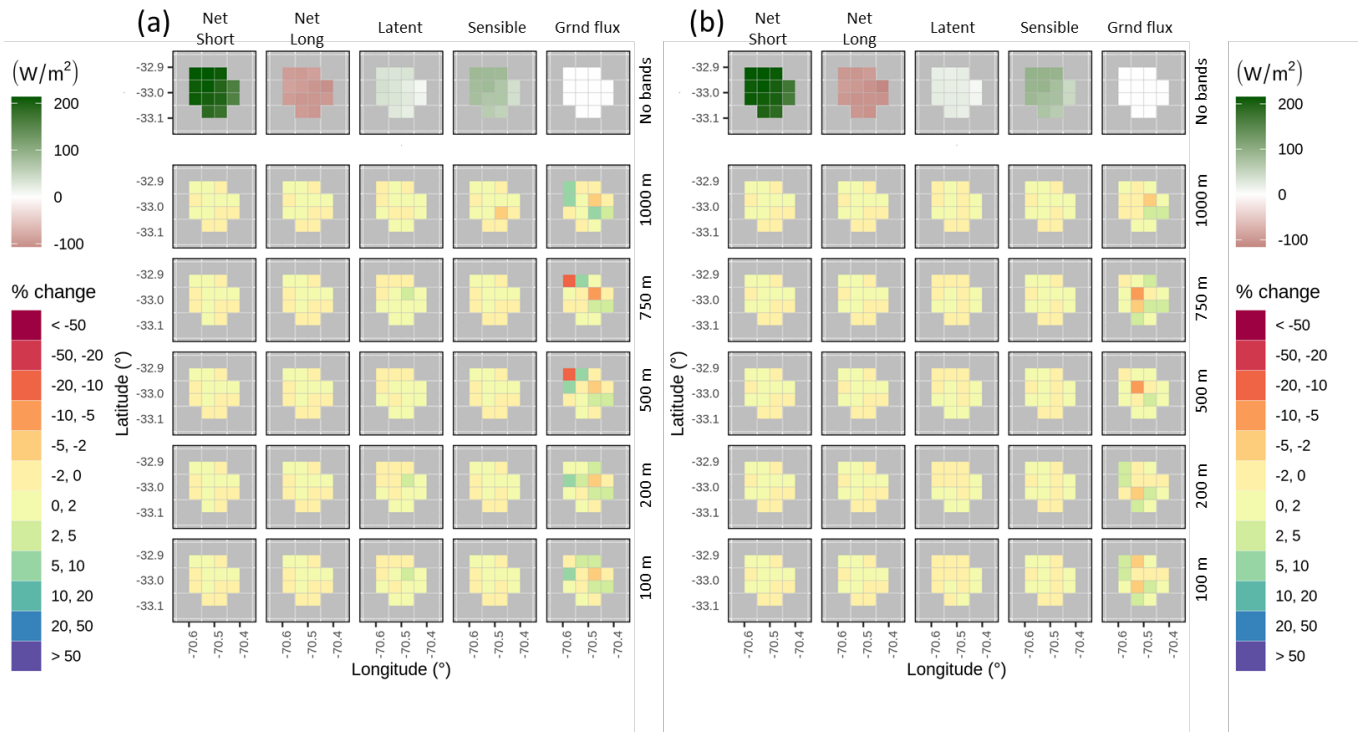

Figure S16: Same as in Figure S15, but for Pocuro en El Sifón.

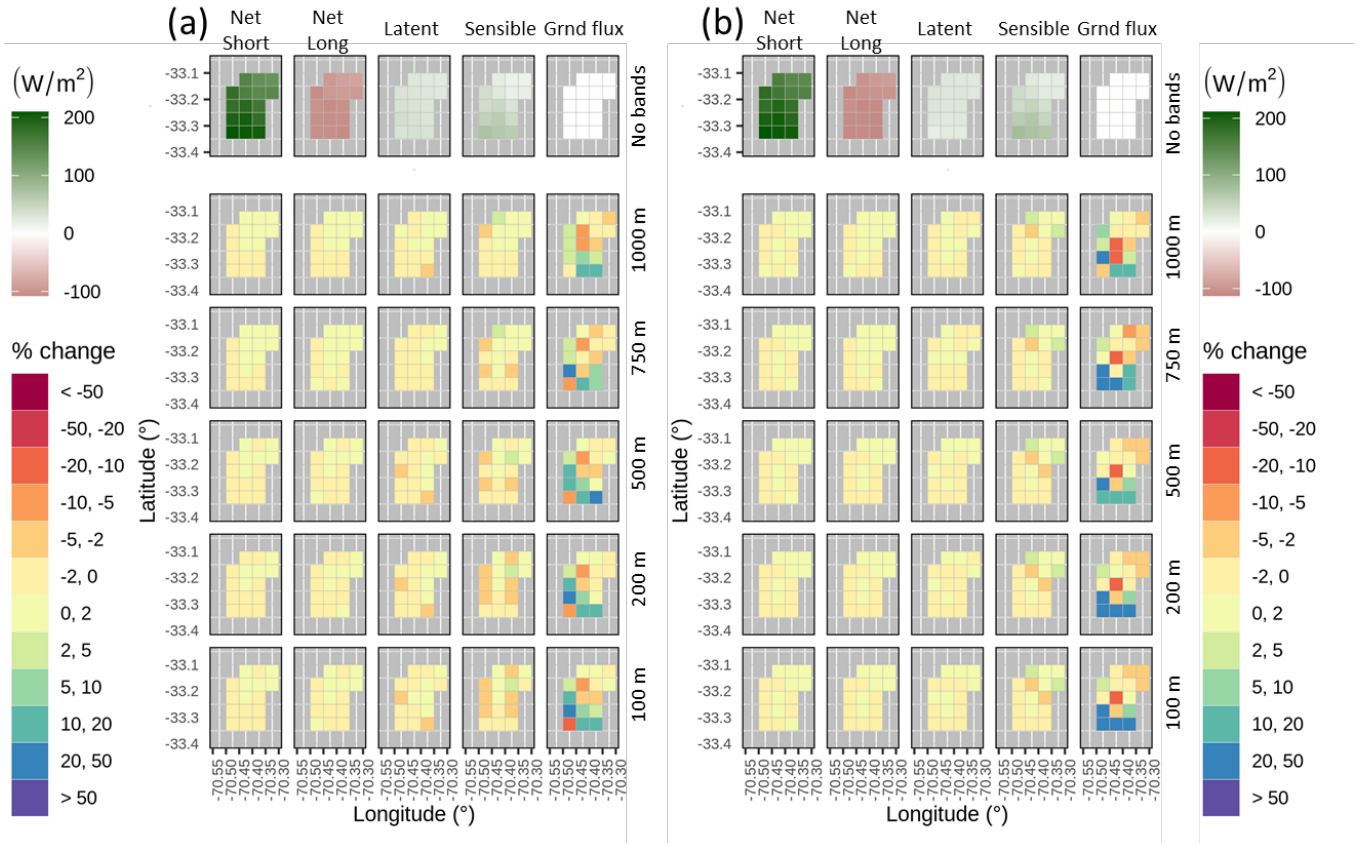

Figure S17: Same as in Figure S15, but for Arrayán en La Montosa.

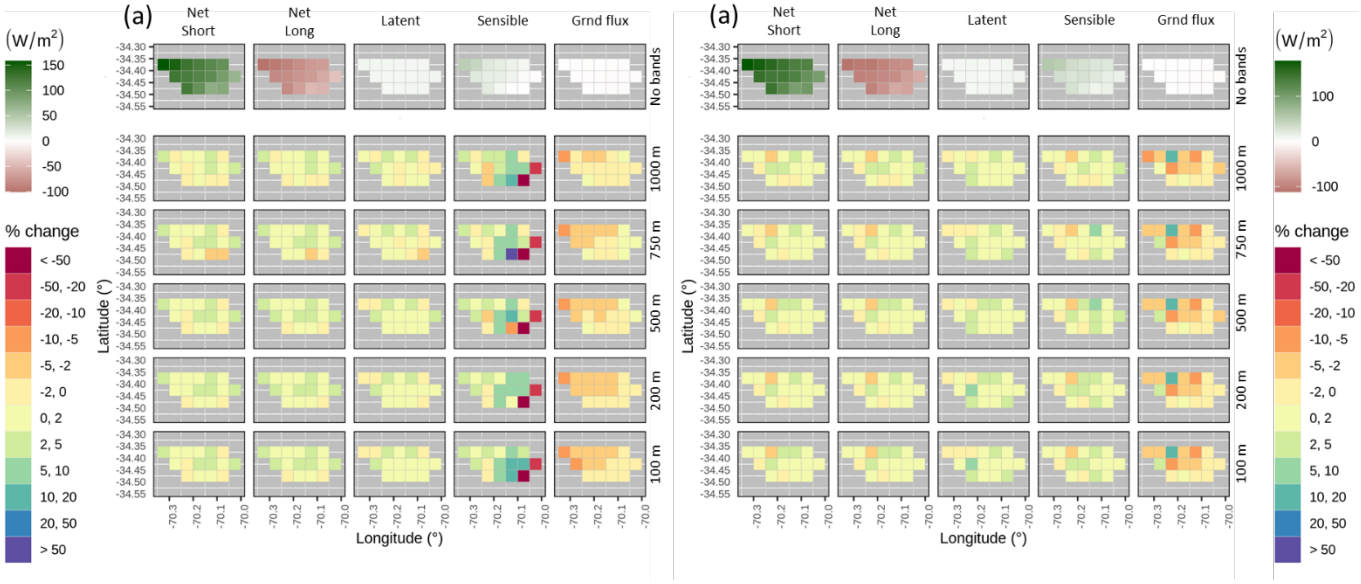

Figure S18: Same as in Figure S15, but for Las Leñas antes junta Río Cachapoal.

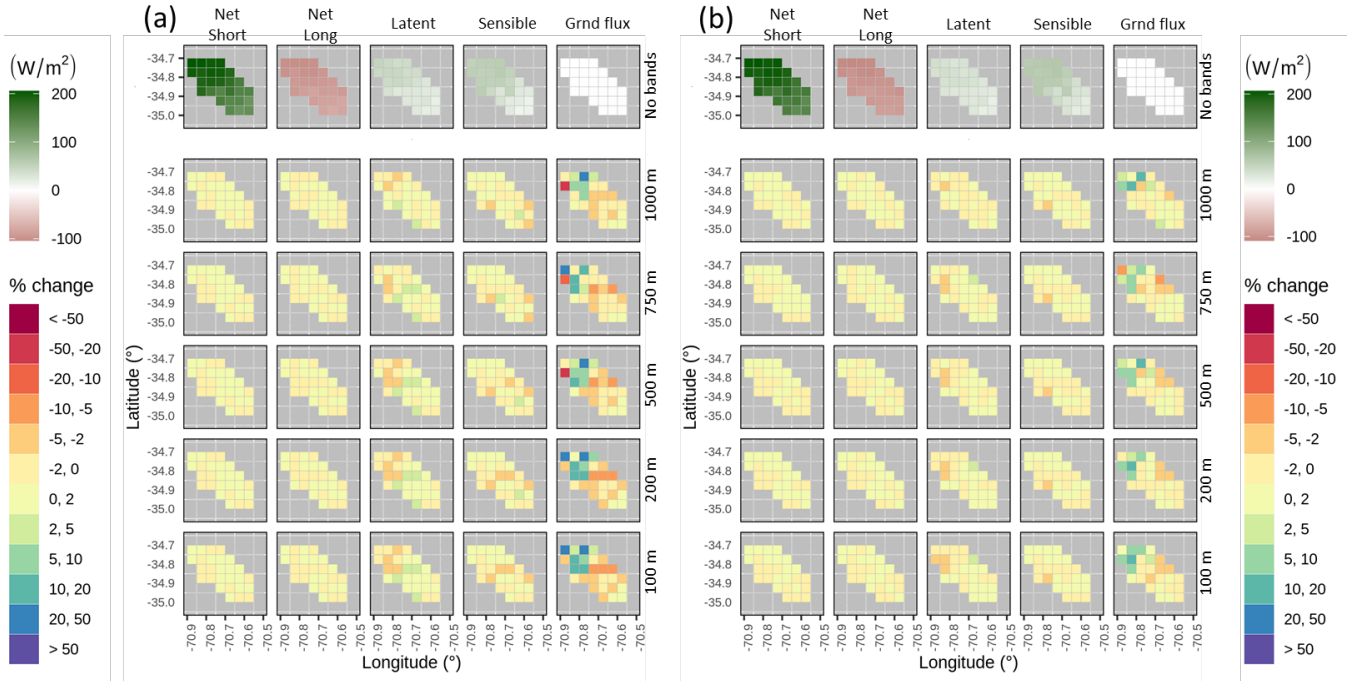

Figure S19: Same as in Figure S15, but for Río Claro en El Valle.

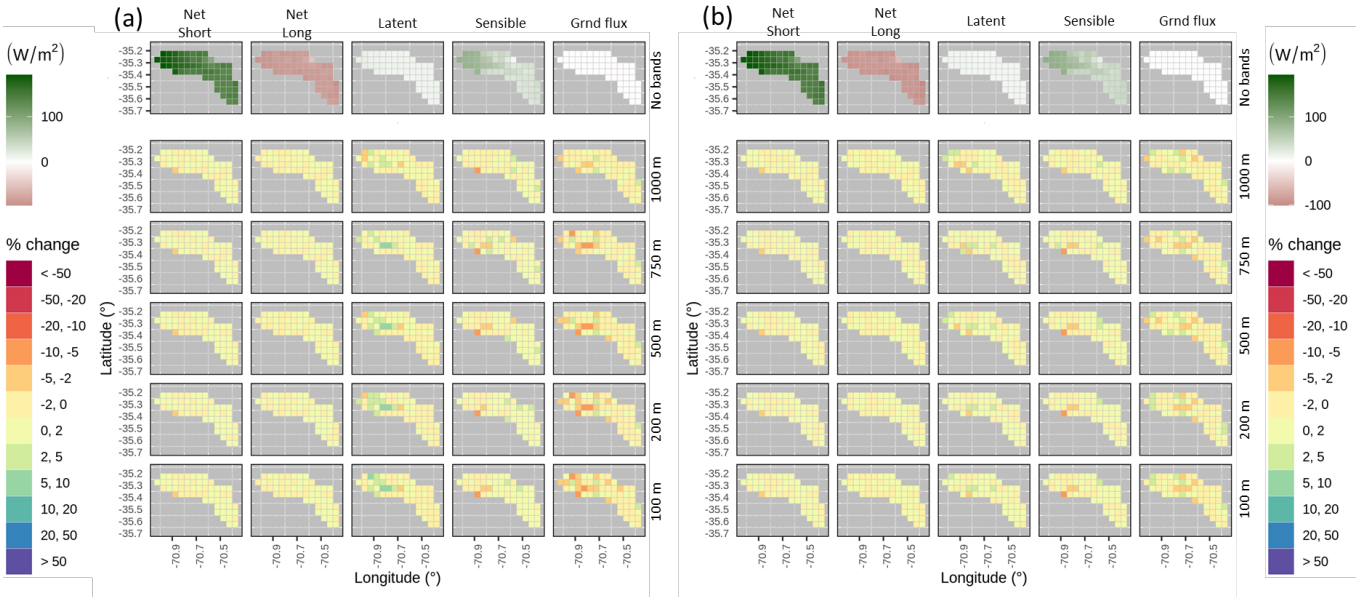

Figure S20: Same as in Figure S15, but for Río Colorado en junta con Palos.

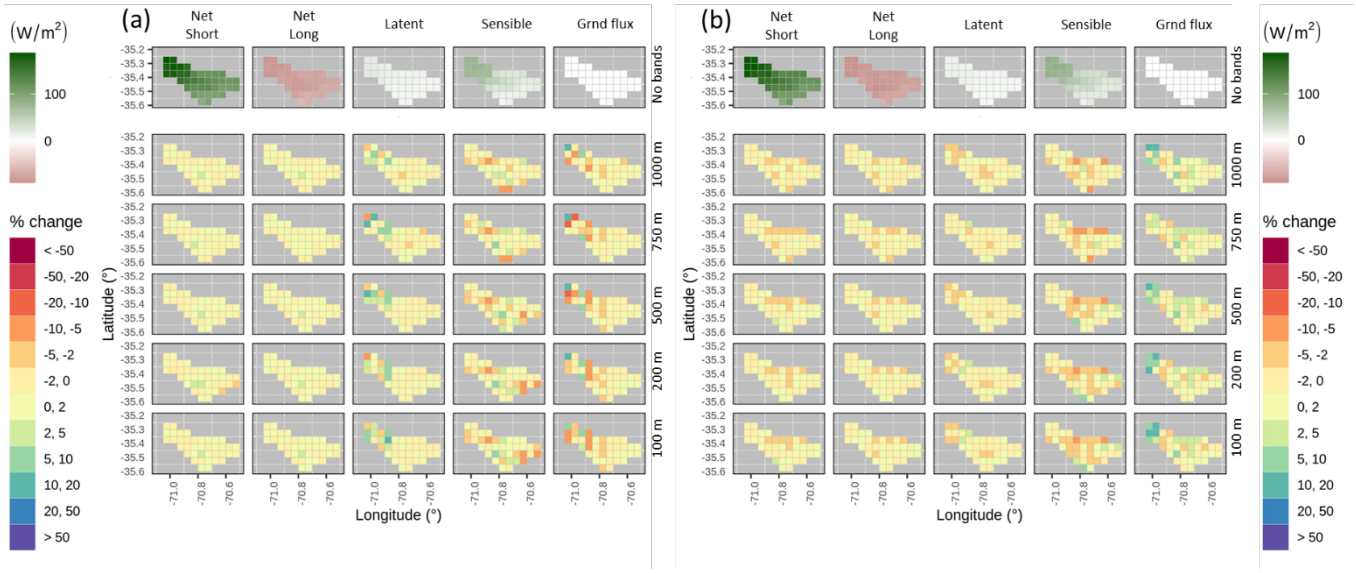

Figure S21: Same as in Figure S15, but for Río Palos en junta con Colorado.

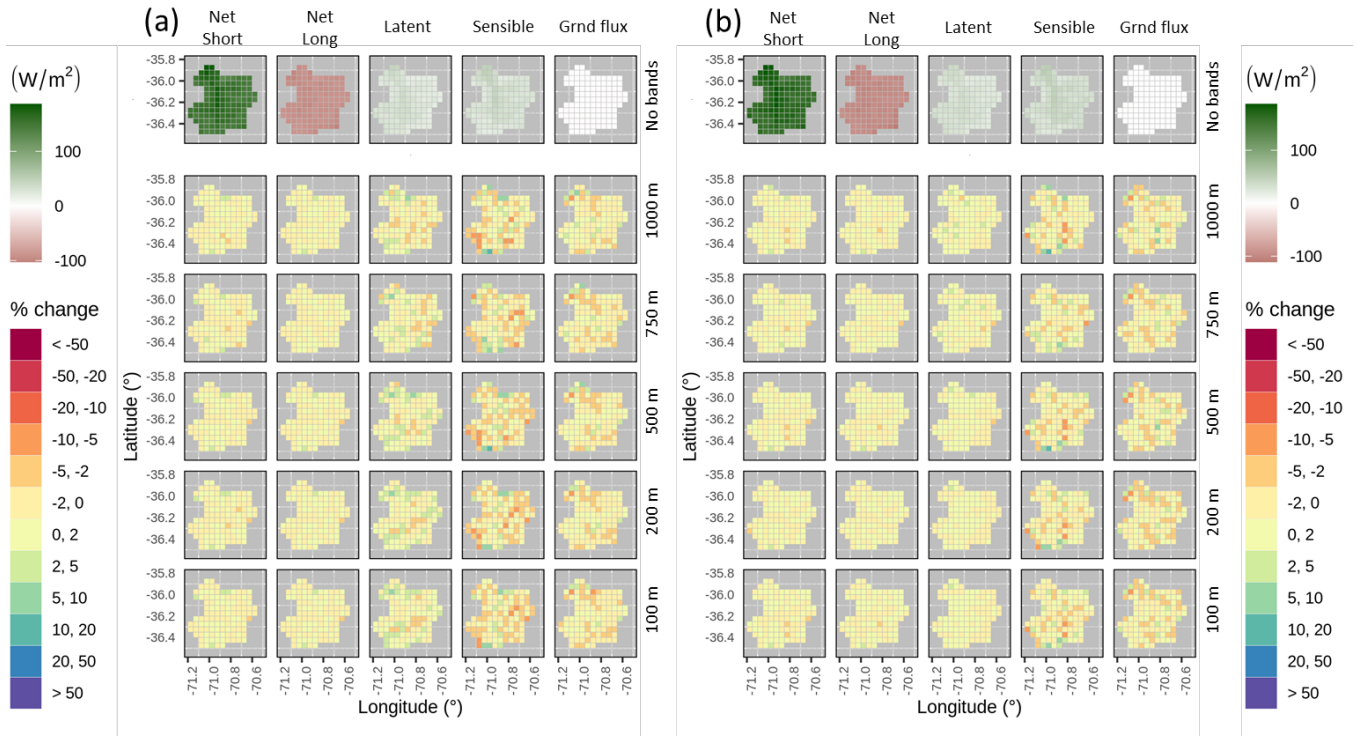

Figure S22: Same as in Figure S15, but for Río Melado en El Salto.

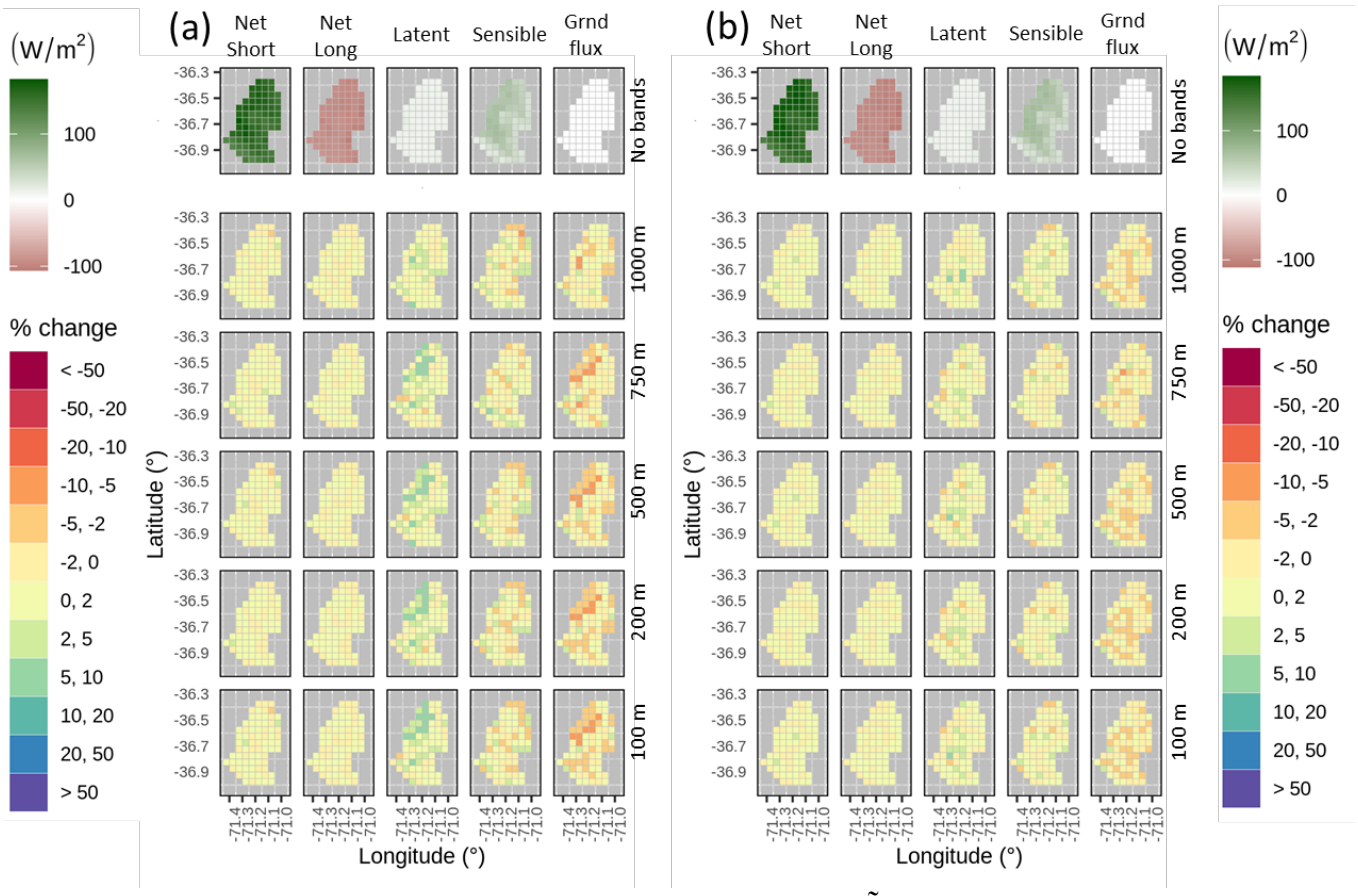

Figure S23: Same as in Figure S15, but for Río Ñuble en La Punilla.

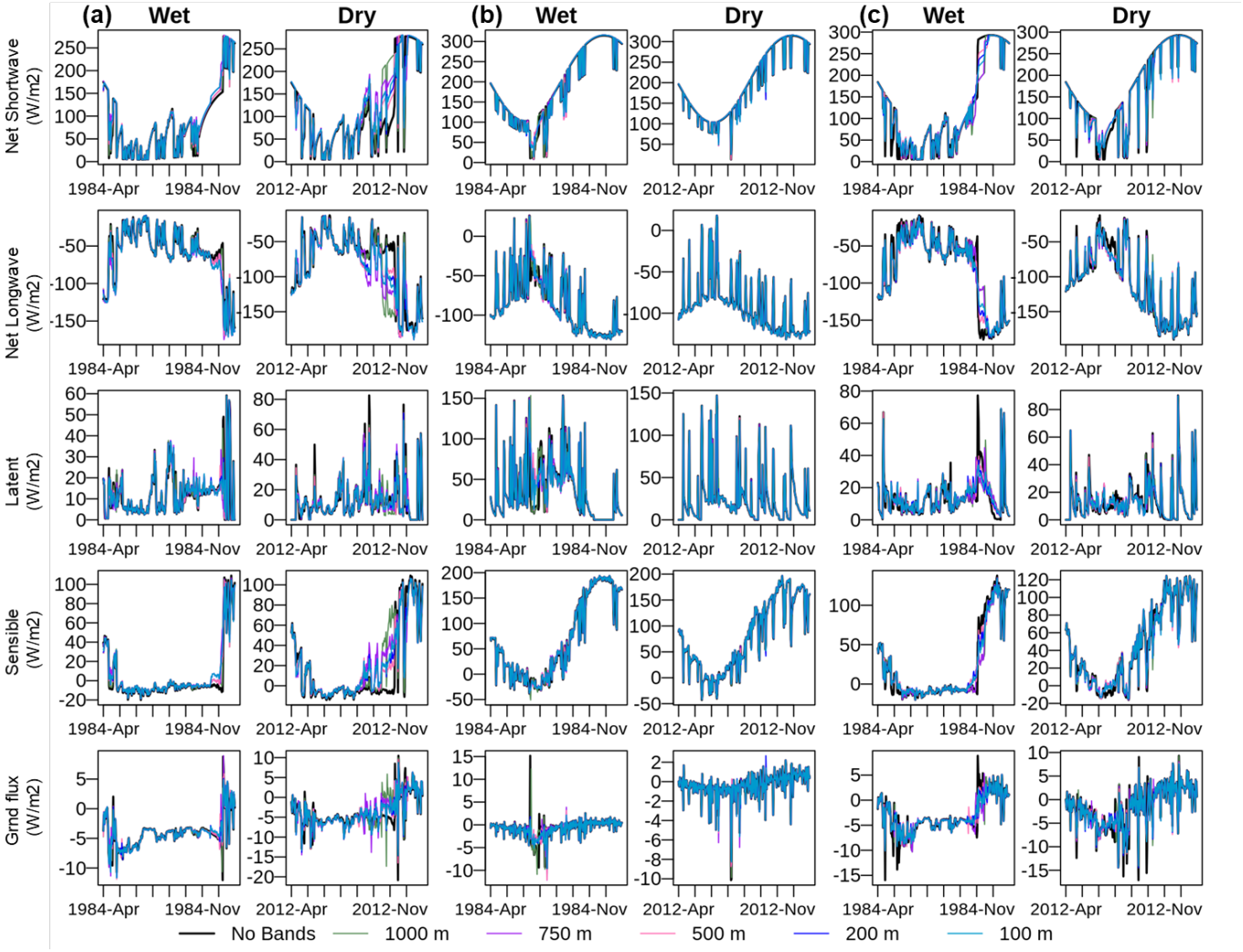

Figure S24: Energy flux variables. Panels (a), (b) and (c) correspond to grid cells (1), (2) and (3) in Figure 3 of the main document. Each column displays results for a snow season belonging to the wet (WY 1984) and dry (WY 2012) subperiods.

References

Bras, R. (1990). *Hydrology: An Introduction to Hydrologic Sciences*. (Addison-Wesley, Ed.).

Deardorff, J. W. (1978). Efficient prediction of ground surface temperature and moisture, with inclusion of a layer of vegetation. *Journal of Geophysical Research*, *83*(C4), 1889. https://doi.org/10.1029/jc083ic04p01889

Thornton, P. E., & Running, S. W. (1999). An improved algorithm for estimating incident daily solar radiation from measurements of temperature, humidity, and precipitation. *Agricultural and Forest Meteorology*, *93*(4), 211–228. https://doi.org/10.1016/S0168-1923(98)00126-9

USACE. (1956). *Snow Hidrology. Summary Report of the Snow Investigations*. Oregon. https://doi.org/92069877